Received: 6 July 2022 | Revised: 3 September 2022 | Accepted: 18 September 2022

IET Electric Power Applications

DOI: 10.1049/elp2.12255

The Institution of Engineering and Technology WILEY

ORIGINAL RESEARCH

Back propagation neural network-based torque ripple reduction strategy for high frequency square-wave voltage injection-based interior permanent magnet synchronous motor sensorless control

Yan Li[1] | Zhen Chen[1] | Xiaoyong Sun[1] | Congzhe Gao[1] | Xiangdong Liu[1] | Youguang Guo[2]

[1]Automation School, Beijing Institute of Technology, Beijing, China

[2]School of Electrical and Data Engineering, University of Technology Sydney, Sydney, New South Wales, Australia

Correspondence

Xiaoyong Sun, Automation School, Beijing Institute of Technology, Beijing 100081, China.
Email: 6120220029@bit.edu.cn

Funding information

National key research and development program, Grant/Award Number: BZ0388202101

Abstract

In interior permanent magnet synchronous motor (IPMSM) position-sensorless drives, the high-frequency (HF) square-wave voltage injection method is often used to estimate the rotor position and speed in low-speed range by tracking the salient polarity of the motor. In order to reduce the torque ripple caused by HF signal injection, a strategy to update the magnitude of the injected signal online by back propagation neural network is proposed in this paper. With the proposed method, the neural network can update the magnitude of the injected signal online according to the *d*-axis current and the position error information. It can not only ensure the accuracy of position extraction but also effectively reduce the current harmonics caused by the injected signal, and then the torque ripple can be reduced. In addition, the proposed method is easy to implement, resulting in low computation burden. Finally, the experiments are implemented on a 1-kW IPMSM drive. The experimental results show that compared with the conventional fixed magnitude injection, the peak-to-peak value of the torque ripple is reduced by nearly half along with the decrease of the injected magnitude.

KEYWORDS

back propagation neural network, interior permanent magnet synchronous motor, sensorless control, square-wave voltage injection method

1 | INTRODUCTION

Interior permanent magnet synchronous motors (IPMSMs) have attracted much attention due to high efficiency, high power density and high torque-to-inertia ratio. To extract the rotor position information, the conventional IPMSM control strategies need to rely on mechanical position sensors, which not only increase the cost of the system but also reduce the power density. Besides, mechanical position sensors are vulnerable to temperature and electromagnetic noise interference, which will greatly reduce the reliability of the IPMSM system. To avoid these problems caused by mechanical position sensors, many position-sensorless control strategies have been developed, which usually extract the rotor position with the aid of some measurable signals such as current responses.

Sensorless control schemes can be broadly divided into two classes [1, 2], that is, the model-based control schemes and the saliency-based control schemes. The first classes rely on the electromotive force (EMF) or the flux associated to the fundamental excitation, which are usually applied in the field of medium-to high-speed range [3–5]. Since the EMF of the IPMSM is proportional to the rotor speed, the application of the model-based methods is limited at low- and zero-speed range [1]. To broaden the sensorless control into low- and zero-speed range, the saliency-based method has been developed, which can be broadly divided into two categories, that is, the injection-based methods and the fundamental pulse width

modulation (PWM) excitation (FPE)-based methods [1]. The former usually injects a specific high-frequency (HF) voltage signal into control ports to induce the HF current responses for the position extraction. While the latter extracts the position information from the responses induced by the fundamental PWM. Compared with the injection-based methods, the FPE-based methods often require additional hardware support or higher accuracy current sensors. Therefore, the injection-based methods could be more attractive.

According to the injection reference frame, the injection-based methods can be roughly subdivided into two categories, that is, the rotating voltage signal injection [6, 7] and the pulsating voltage signal injection. Moreover, the waveforms of the injected HF signal can be generally classified as the sine-wave signal [6–9], the square-wave signal [10–13], and the random-wave signal [15–17].

At present, many researchers have carried out in-depth study on the injection-based methods. On one hand, researchers pay much attention to the dynamic performance improvement of sensorless control [3]. To extend the bandwidth of speed and current controllers, Sul et al. [10] are the first to propose the square-wave voltage injection method. The low-pass filters (LPFs), which should be used to get the position error signal, are removed. To further enhance the position estimation performance, Kwon and Sul [11] analyse and compensate the inverter non-linearity during the injection by connecting additional capacitors. Moreover, with the new inverter topology, the magnitude of the injected signal can also be reduced by more than half. Some researchers focus on enhancing the speed loop regulator to get better sensorless control performance. Ref. [12, 13] propose the active disturbance rejection control (ADRC) strategy-based and the enhanced linear ADRC strategy-based sensorless control schemes, respectively. The total disturbance in the sensorless drive is estimated by the extended state observer (ESO) and compensated by a non-linear error feedback controller. Furthermore, some researchers try to develop novel injection strategies to improve the sensorless control dynamic performances. For instance, the literature in Ref. [14] injected the HF signal into the ABC reference frame, which can not only accurately obtain the rotor position information but also achieve good steady state and dynamic performances.

On the other hand, owing to the HF signal injection, the HF current response suffers from HF harmonics, which will cause additional torque ripple and losses. Thus, many researchers also focus on compensating the negative influences of the injection-based methods, especially, the torque ripple. The existing methods for suppressing the torque ripple mainly focus on the optimisation of motor design [18–20] and the improvement of control strategies [21–23]. Different from the conventional sensorless control strategy with single HF signal injected into the d-axis, Ref. [21] chooses a special voltage vector composed by both d- and q-axis HF signals. It has been confirmed that the HF current responses will cause the minimum torque ripple when the total magnitude of the injected composite signal is definite. Similar to Ref. [21], the literature in Ref. [22] proposes a bi-axis HF signal injection (Bi-HFSI) scheme, which can broaden the torque spectrum so as to decrease the HF torque ripple. Both of these methods mentioned before take full account of the characteristics of the motor whose torque is affected by both d- and q-axis current responses. However, the magnitude of the injected signal is supposed to be as low as possible and how to select an appropriate magnitude of the injected signal is not presented. The literature in Ref. [23] also proposes a novel HF injection method, which mainly focusses on reducing the influence of the inverter non-linearity by regulating the HF current ripple. Although the current response performance is improved, sufficient results of the torque ripple reduction are not presented.

It is noted that the torque performance is affected by the additional signal injection, which can be relieved by reducing the magnitude of the injected signal [11]. However, the magnitude of the injected signal cannot be reduced under a certain value due to the inverter non-linearity [11, 23]. Moreover, in practical application, the injected magnitude margin should be further discussed considering the quantisation error of current sensors and undesirable disturbances. Therefore, the injected signal with an adaptive magnitude could be a good choice, and the magnitude is adjusted online according to the motor operation condition.

This paper proposes a strategy to find the optimal magnitude of the injected signal for torque ripple reduction in square-wave voltage injection-based IPMSM sensorless control. Different from the existing injection methods, this scheme adopts a signal with variable magnitude and the magnitude is updated online by a three-layer back propagation neural networks (BPNNs). The inputs of the BPNN are the d-axis current and position estimation error related parameters while the output of the BPNN is treated as the magnitude of the injected signal. With this kind of BPNN structure, the BPNN could strive to reduce the magnitude of the signal while keeping sufficient accuracy of the position estimation. In addition, this scheme occupies a small amount of controller resources.

This paper is organised as follows. Section 2 introduces the conventional sensorless control strategy based on the square-wave HF signal injection. In Section 3, the construction of the BPNN-based optimal injection method is introduced and the stability of the BPNN is analysed. Section 4 compares the experimental results of the conventional and the proposed methods to illustrate the effectiveness of the proposed method. Finally, Section 5 makes the conclusion of this paper.

2 | CONVENTIONAL SQUARE-WAVE VOLTAGE INJECTION-BASED IPMSM SENSORLESS CONTROL AT LOW- AND ZERO-SPEED RANGE

2.1 | Control block diagram

Figure 1 shows the conventional HF square-wave voltage injection-based IPMSM sensorless control block diagram. In this paper, Field-Oriented Control (FOC) is adopted as the control strategy for the closed-loop system. In order to achieve

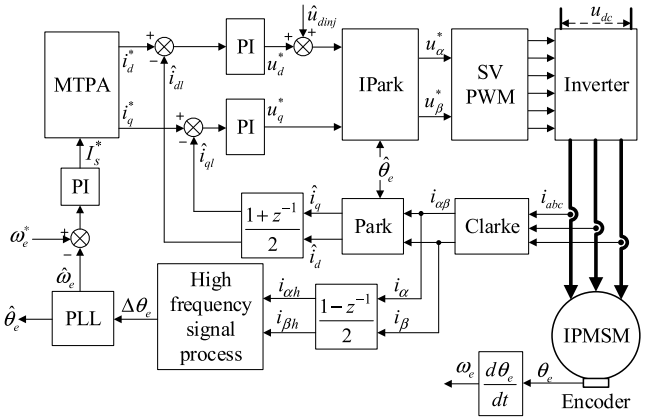

FIGURE 1 Conventional high frequency (HF) square-wave voltage injection-based interior permanent magnet synchronous motor (IPMSM) sensorless control block diagram

optimal torque performance, the maximum torque per ampere (MTPA) control strategy based on lookup tables is adopted and it can be obtained from numerical analysis.

2.2 | Mathematical model

In d-q reference frame, the voltage model of IPMSM can be expressed as

$$\begin{bmatrix} u_d \\ u_q \end{bmatrix} = \begin{bmatrix} R_s + pL_d & -\omega_e L_q \\ \omega_e L_d & R_s + pL_q \end{bmatrix} \begin{bmatrix} i_d \\ i_q \end{bmatrix} + \begin{bmatrix} 0 \\ \omega_e \psi_f \end{bmatrix} \tag{1}$$

where u_d and u_q are the stator voltage components of d-q axis. i_d and i_q are the stator current components of d-q axis. R_s is the stator resistance. L_d and L_q are the d-q axis inductances. ω_e is the electrical speed of motor. ψ_f is the permanent magnet flux linkage and p is the differential operator.

The electromagnetic torque of IPMSM can be expressed as

$$T_e = n_p \left[\psi_f i_q + (L_d - L_q) i_q i_d \right] \tag{2}$$

where T_e represents the electromagnetic torque and n_p is the number of pole pairs.

Since the frequency of the injected signal is much higher than the IPMSM fundamental operation frequency at low- and zero-speed range, the terms associated with the stator resistance and the electrical speed can be neglected. Then, Equation (1) can be further derived as

$$\begin{bmatrix} u_{dh} \\ u_{qh} \end{bmatrix} = \begin{bmatrix} L_d & 0 \\ 0 & L_q \end{bmatrix} p \begin{bmatrix} i_{dh} \\ i_{qh} \end{bmatrix} \tag{3}$$

$$\begin{bmatrix} u_{\alpha h} \\ u_{\beta h} \end{bmatrix} = \begin{bmatrix} L_0 + L_1 \cos(2\theta_e) & L_1 \sin(2\theta_e) \\ L_1 \sin(2\theta_e) & L_0 - L_1 \cos(2\theta_e) \end{bmatrix} p \begin{bmatrix} i_{\alpha h} \\ i_{\beta h} \end{bmatrix} \tag{4}$$

where $L_0 = (L_d + L_q)/2$ and $L_1 = (L_d - L_q)/2$. u_{dh} and u_{qh} are the HF stator voltage components of d-q axis. i_{dh} and i_{qh} are the HF stator current components of d–q axis. $u_{\alpha h}$ and $u_{\beta h}$ are the HF stator voltage components of α–β axis. $i_{\alpha h}$ and $i_{\beta h}$ are the HF stator current components of α–β axis. θ_e is the electrical rotor angle.

The injected HF square wave voltage can be described as

$$\begin{aligned} \hat{u}_{dinj} &= \begin{cases} V_h, & \text{half duty of PWM} \\ -V_h, & \text{otherwise} \end{cases}, (V_h > 0) \\ \hat{u}_{qinj} &= 0 \end{aligned} \tag{5}$$

where symbol "^" means the components of the estimated rotor reference frame. $\hat{u}_{dinj}$ and $\hat{u}_{qinj}$ represent the d- and q-axis injected signals, respectively. V_h is the magnitude of the injected signal.

According to Equations (4) and (5), the relationship between the induced HF currents ($i_{\alpha h}$, $i_{\beta h}$) and the injected voltage $\hat{u}_{dinj}$ in the stationary reference frame can be described as

$$\begin{bmatrix} i_{\alpha h} \\ i_{\beta h} \end{bmatrix} = \int \hat{u}_{dinj}\, dt \begin{bmatrix} \dfrac{\cos(\theta_e)\cos(\Delta\theta)}{L_d} + \dfrac{\sin(\theta_e)\sin(\Delta\theta)}{L_q} \\ \dfrac{\sin(\theta_e)\cos(\Delta\theta)}{L_d} - \dfrac{\cos(\theta_e)\sin(\Delta\theta)}{L_q} \end{bmatrix} \tag{6}$$

where $\Delta\theta_e = \theta_e - \hat{\theta}_e$ is the position error.

Supposing $\Delta\theta_e$ is small enough, Equation (5) can be derived as

$$\begin{bmatrix} i_{\alpha h} \\ i_{\beta h} \end{bmatrix} = \frac{\int \hat{u}_{dinj} dt}{L_d} \begin{bmatrix} \cos(\theta_e) \\ \sin(\theta_e) \end{bmatrix} \tag{7}$$

Equation (7) reveals that the rotor position is contained in the HF current responses in the stationary reference frame. To extract the rotor position, Equation (7) needs to be demodulated further as shown in Figure 2a. Then, let $K(\Delta\theta_e)$ represent the demodulated signal in which the rotor position and speed can be extracted by the phase-locked loop (PLL). Figure 2b shows the typical PID-type PLL. K_1, K_2 and K_3 are the coefficients of the PLL. $\hat{J}_{eq}$ represents the equivalent moment of inertia.

The HF current responses can be further derived in the estimated rotating reference frame as

$$\begin{bmatrix} \hat{i}_{dh} \\ \hat{i}_{qh} \end{bmatrix} = \frac{\int \hat{u}_{inj} dt}{L_d L_q} \begin{bmatrix} L_0 - L_1 \cos(2\Delta\theta_e) \\ -L_1 \sin(2\Delta\theta_e) \end{bmatrix} \tag{8}$$

where $\hat{i}_{dh}$ and $\hat{i}_{qh}$ are the HF current responses in the estimated rotating reference frame, respectively.

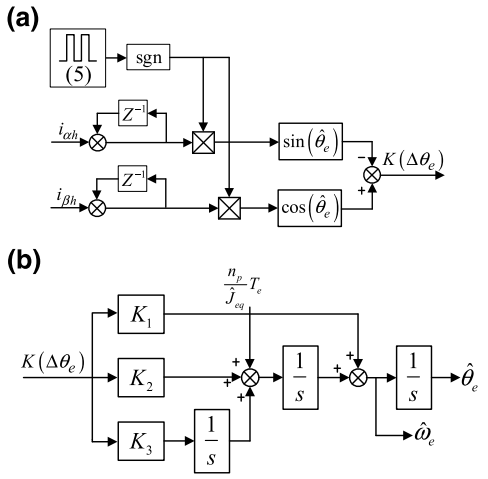

FIGURE 2 High frequency signal process. (a) Signal demodulation. (b) PID-type phase-locked loop (PLL)

Supposing $\Delta\theta_e$ is small enough, $\widehat{i}_{qh}$ tends to zero. Therefore, the electromagnetic torque accounting for the influence of the HF signal injection can be further expressed as

$$T_e = n_p\left[\psi_f\left(i_q+\widehat{i}_{qh}\right)+\left(L_d-L_q\right)\left(i_q+\widehat{i}_{qh}\right)\left(i_d+\widehat{i}_{dh}\right)\right]$$
$$\approx \underbrace{n_p\left[\psi_f i_q+\left(L_d-L_q\right)i_q i_d\right]}_{1}+\underbrace{n_p\left(L_d-L_q\right)i_q\widehat{i}_{dh}}_{2} \quad (9)$$

It can be found from Equation (9) that the part 2, especially the $\widehat{i}_{dh}$ is the primary factor for introducing the additional torque ripple. It is noted that a large injection magnitude could introduce more torque ripple. While a small magnitude of the injected signal is unfavourable to the precision of position observation due to the accuracy of current sensors. Therefore, it is important to balance the performance between the torque ripple reduction and the position observation.

Different from the conventional control strategy with a fixed injection magnitude, a BPNN-based control strategy is developed in this paper to obtain the optimal magnitude of the injected signal according to the motor operation condition. The proposed control method can not only guarantee the accuracy of position extraction but also reduce the torque ripple caused by the HF current responses as much as possible.

3 | PROPOSED BPNN-BASED IPMSM SENSORLESS CONTROL FOR TORQUE RIPPLE REDUCTION

This section introduces the proposed method, which calculates the optimal magnitude of the injected signal based on the BPNN. Figure 3 shows the control block diagram of the proposed method. Different from the conventional schemes, the proposed method adopts a variable injection magnitude V_h,

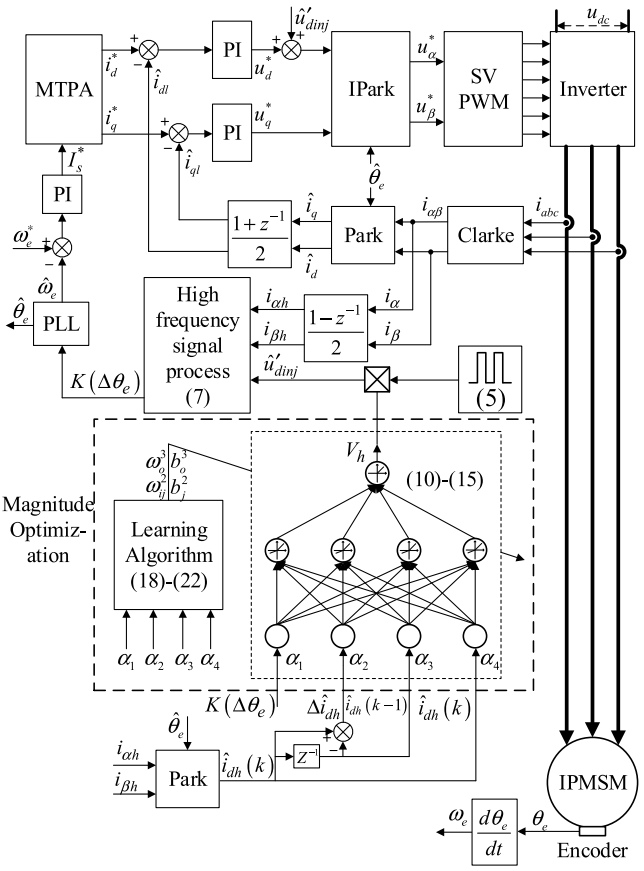

FIGURE 3 Control block diagram of the proposed method

which is calculated by the proposed BPNN, as highlighted in Figure 3. The parameters of the BPNN are updated by the online learning algorithm based on the back propagation. To guarantee the accuracy of position estimation, the demodulated signal $K(\Delta\theta_e)$ is adopted as one of the inputs of the BPNN. The other inputs are related to the d-axis HF current response $\widehat{i}_{dh}$. The k th and (k-1)th sample instants of $\widehat{i}_{dh}$ are adopted to reduce the torque ripple and the difference between k th and (k-1)th sample instants $\Delta\widehat{i}_{dh}$, that is, $\Delta\widehat{i}_{dh}=\widehat{i}_{dh}(k)-\widehat{i}_{dh}(k-1)$ is considered to enhance the disturbance-rejection capability under load change. Moreover, the injection-based sensorless control is applicable to the low- and zero-speed range. Therefore, the applicability of the proposed method for medium- and high-speed range is not considered in this paper.

The details of the proposed method are introduced as follows.

3.1 | STRUCTURE OF THE BPNN

The structure of the BPNN is shown in Figure 4.

The basic function and the signal propagation in each layer are introduced as follows:

(1) Layer 1: The Input Layer. In this layer, the input and output of each node can be described as follows:

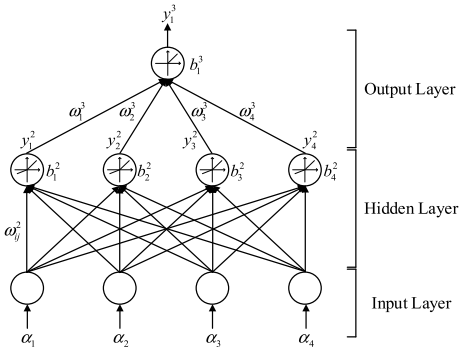

FIGURE 4 Proposed network structure

$$\text{node}_i^1(k) = x_i^1(k), \quad i = 1,2,3,4 \tag{10}$$

$$y_i^1(k) = f_i^1\left(\text{node}_i^1(k)\right) = \text{node}_i^1(k) \tag{11}$$

where x_i^1 is the input of the ith node in this layer. y_i^1 represents the output of the ith node. $f_i^1(\cdot)$ represents a unity function of the ith node. K represents the kth sample time.

Define the inputs of the BPNN as

$$\begin{aligned} \alpha_1(k) &= K(\Delta\theta_e) \\ \alpha_2(k) &= \Delta\widehat{i}_{dh} = \widehat{i}_{dh}(k) - \widehat{i}_{dh}(k-1) \\ \alpha_3(k) &= \widehat{i}_{dh}(k-1) \\ \alpha_4(k) &= \widehat{i}_{dh}(k) \end{aligned} \tag{12}$$

where $K(\Delta\theta_e)$ represents the demodulated signal shown in Figure 2. $\widehat{i}_{dh}$ is the d-axis HF current response shown in Equation (8).

(2) Layer 2: The Hidden Layer. In this layer, the Leaky rectified linear unit (ReLU) function is adopted as the activation function so as to accelerate convergence. Then, the input and output can be described as follows:

$$\text{node}_j^2(k) = \sum_i \left(\omega_{ij}^2(k) x_j^2(k)\right) + b_j^2(k), \quad j = 1,2,3,4 \tag{13}$$

$$y_j^2 = f_j^2\left(\text{node}_j^2(k)\right) = \begin{cases} \text{node}_j^2(k) & \text{if } \text{node}_j^2(k) > 0 \\ a_2 \text{node}_j^2(k) & \text{if } \text{node}_j^2(k) \le 0 \end{cases} \tag{14}$$

where $x_j^2 = y_i^1(k)$ is the input of this layer. ω_{ij}^2 and b_j^2 are the weights and bias of the j^{th} node associated with the i^{th} input variable, respectively. y_j^2 represents the output of the j^{th} node. $f_j^2(\cdot)$ represents a unity function of the j^{th} node, and a_2 represents a constant value. $f_j^2\left(\text{node}_j^2(k)\right)$ represents the L-ReLU function output.

(3) Layer 3: The Output Layer. The output of this layer is adopted as the magnitude of the injected HF signal, which should always be positive. Therefore, the non-negative ReLU function is adopted as the activation function. Then, the input and output can be described as follows:

$$\text{node}_o^3(k) = \sum_j \left(\omega_{jo}^3(k) x_o^3(k)\right) + b_o^3(k), \quad o = 1 \tag{15}$$

$$y_o^3 = f_o^3\left(\text{node}_o^3(k)\right) = \begin{cases} \text{node}_o^3(k) & \text{if } \text{node}_o^3(k) > 0 \\ 0 & \text{if } \text{node}_o^3(k) \le 0 \end{cases} \tag{16}$$

where $x_o^3 = y_j^2(k)$ is the input of this layer. ω_{jo}^3 and b_o^3 are the weights and bias of the o^{th} node associated with the j^{th} input variable, respectively. $y_o^3(k)$ represents the output of the o^{th} node. $f_o^3(\cdot)$ represents a unity function of the o^{th} node. $f_o^3\left(\text{node}_o^3\right)$ represents the non-negative ReLU function output.

3.2 | Online learning algorithm

The gradient decent method is adopted to describe the online learning algorithm. Then, the energy function can be defined as follows [24]:

$$V(k) = \frac{1}{2}\left[(\alpha_1(k))^2 + (\alpha_2(k))^2 + (\alpha_3(k))^2 + (\alpha_4(k))^2\right] \tag{17}$$

The learning algorithm can be described as follows:

Layer 3: The error term to be propagated is given by:

$$\delta_o^3 = \frac{\partial V(k)}{\partial \text{node}_o^3(k)} = \frac{\partial V(k)}{\partial y_o^3(k)} \frac{\partial y_o^3(k)}{\partial \text{node}_o^3(k)} \tag{18}$$

The connective weights ω_{jo}^3 and bias b_o^3 are updated as follows:

$$\begin{aligned} \omega_{jo}^3(k) &= \omega_{jo}^3(k-1) + \eta_3 \delta_o^3 \dot{y}_o^3(k) \\ b_o^3(k) &= b_o^3(k-1) + \eta_3 \delta_o^3 \end{aligned} \tag{19}$$

where η_3 is the learning rate of layer 3.

Layer 2: The error term to be propagated is calculated as follows:

$$\begin{aligned} \delta_j^2 &= \left(\omega_{jo}^3(k)\right)^T \delta_o^3 \frac{\partial V(k)}{\partial \text{node}_j^2(k)} \\ &= \left(\omega_{jo}^3(k)\right)^T \delta_o^3 \frac{\partial V(k)}{\partial \text{node}_o^3(k)} \frac{\partial \text{node}_o^3(k)}{\partial \text{node}_j^2(k)} \end{aligned} \tag{20}$$

Then the connective weights ω_{ij}^2 and bias b_j^2 are updated as follows:

$$\begin{aligned} \omega_{ij}^2(k) &= \omega_{ij}^2(k-1) + \eta_2 \delta_j^2 \dot{y}_j^2(k) \\ b_j^2(k) &= b_j^2(k-1) + \eta_2 \delta_j^2 \end{aligned} \tag{21}$$

where η_2 is the learning rate of layer 2.

Due to the uncertainty of the IPMSM drive, the exact value of the terms contained in $\partial V / \partial \text{node}_o^3$ cannot be calculated directly. According to Ref. [24], this problem can be relieved by

adopting the delta adaptation law [25], which can be represented as follows:

$$\delta_o^3 = \alpha_1(k) + \alpha_2(k) + \alpha_3(k) + \alpha_4(k) \tag{22}$$

Then, the introduction of the learning algorithm is complete.

3.3 | Stability analysis

The main point of selecting the learning rate is to guarantee the convergence of the BPNN. Therefore, the analysis of the aforementioned discrete-type Lyapunov function should be considered. Then, the learning rate can be derived as follows:

$$\begin{aligned} \eta_3 &= \frac{V(k)/2}{Q_3 + \varepsilon} \\ \eta_2 &= \frac{V(k)/2}{Q_2 + \varepsilon} \end{aligned} \tag{23}$$

$$\begin{aligned} Q_3 &= \left(\frac{\partial V(k)}{\partial \text{node}_o^3(k)} \frac{\partial \text{node}_o^3(k)}{\partial \omega_{jo}^3(k)} \right)^2 \\ Q_2 &= \sum_{j=1}^{4} \left(\frac{\partial V(k)}{\partial \text{node}_j^2(k)} \frac{\partial \text{node}_j^2(k)}{\partial \omega_{ij}^2(k)} \right)^2 \end{aligned} \tag{24}$$

where ε is a small positive integer.

Transferring the energy function in Equation (16) as a discrete-type Lyapunov function, it can be written as follows:

$$\Delta V(k) = V(k+1) - V(k) \tag{25}$$

Then, the energy function can be derived as

$$\begin{aligned} V(k+1) &= V(k) + \Delta V(k) \\ &\approx V(k) + \left[\frac{\partial V(k)}{\partial \omega_{jo}^3(k)} \Delta \omega_{jo}^3(k) \right] \\ &\quad + \sum_{j=1}^{4} \left[\frac{\partial V(k)}{\partial \omega_{ij}^2(k)} \Delta \omega_{ij}^2(k) \right] \\ &= \frac{V(k)}{2} - \eta_3 \left[\frac{\partial V(k)}{\partial \text{node}_o^3(k)} \frac{\partial \text{node}_o^3(k)}{\partial \omega_{jo}^3(k)} \right]^2 \\ &\quad + \frac{V(k)}{2} - \eta_2 \sum_{j=1}^{4} \left[\frac{\partial V(k)}{\partial \text{node}_j^2(k)} \frac{\partial \text{node}_j^2(k)}{\partial \omega_{ij}^2(k)} \right]^2 \end{aligned} \tag{26}$$

Substituting the learning rate shown in Equation (23) into Equation (26), the following result can be obtained:

$$V(k+1) < V(k) \tag{27}$$

Then the proof of convergence of system is complete.

4 | EXPERIMENTAL RESULTS

To perform a fair comparison, the experiments of the conventional and the proposed methods are all based on the same test rig and under the same conditions. The only difference is that the conventional method adopts a fixed injection magnitude while the proposed method employs an optimal injection magnitude based on the BPNN structure. The details of the experimental setup and results are introduced as follows.

All the experiments have been verified on a 3 kW IPMSM drive using a DSP/FPGA-based control board as shown in Figure 5 and the basic parameters of the tested IPMSM are listed in Table 1.

A Texas Instruments TMS320F28335 DSP and an Altera EP3C25Q240C8n FPGA are adopted in this experiment. The DSP is adopted to execute the proposed algorithm and the FPGA is in charge of outputting the control waveform. The frequency of the IGBT switching is set as 10 kHz, and the FOC is adopted as the control strategy during the IGBT switching periods. In order to obtain better operation performance, the bandwidth of the speed regulator will not be set too large [1]. In addition, the rotor position will be extracted by the PLL whose inputs should be normalised since the poles of the PLL may change at different speeds without normalisation. The normalisation process can be expressed in Figure 6.

In the following experiments, the frequency of the injected HF signal is set as 5 kHz, that is, half of the PWM frequency. For comparison, the conventional method adopts a fixed magnitude of injected signal, while in the proposed method, the magnitude is calculated by the BPNN. Moreover, when the motor runs in low-speed range, the fundamental frequency of motor is much lower than the switching frequency. In other words, the injected signal does not need to be updated frequently. In this paper, the update frequency of the injected signal is set as 1 kHz. Accounting for the computation burden and the controller resources, the total BPNN algorithm can be divided into 10 steps, that is, S1-10 shown in Figure 7. In every control period, only one executed step is contained. The computing time of each step is also shown in Figure 7. Therefore, the proposed method will not result in a lot of computation burden. Furthermore, the output of the BPNN needs to be limited within a certain range for avoiding the extreme disturbance such as the locked rotor, which will worsen control performance. In this paper, the output of the BPNN is limited within 0–20 V.

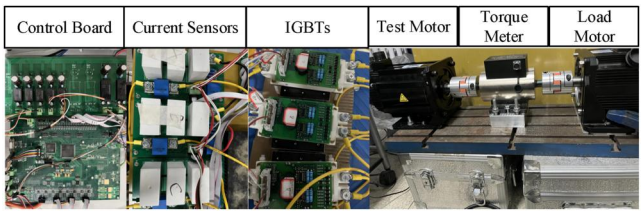

FIGURE 5 Experimental setup

TABLE 1 Basic parameters of interior permanent magnet synchronous motor (IPMSM)

Parameters	IPMSM
Rated power	3.0 kW
Rated speed	2000 rpm
Rated current	14.6 A
Rated torque	12.7 Nm
Phase resistance	0.23 Ω
d-axis inductance	1.96 mH
q-axis inductance	2.38 mH
Pole pairs	5
DC-link voltage	220 V

Abbreviation: IPMSM, interior permanent magnet synchronous motor

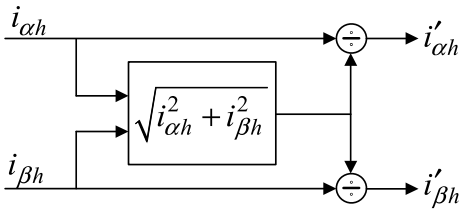

FIGURE 6 Normalisation of currents

4.1 | Motor start-up with step load change

Figures 8, 9 and 10 show the comparison between the conventional sensorless control method and the proposed method at motor start-up with step load change. In these three experiments, the motor starts up from 0 to 150 rpm with a light load of 2 nm and the load changes to 11 nm after the motor runs at steady-state. The results in each group contains five aspects, which are the rotor speed, the rotor position, the position error, the magnitude of the injected signal and the electromagnetic torque performance, and the phase currents (phase A and B) responses, respectively. The only different among the three conditions is the magnitude of injected signal, that is, Figures 8 and 9 adopt 10 and 15 V, respectively, while Figure 10 adopts the magnitude calculated by the proposed BPNN.

First, it can be seen from Figures 8 and 9 that in terms of the performance of position tracking, both of them can track the rotor position precisely at steady-state and both of the

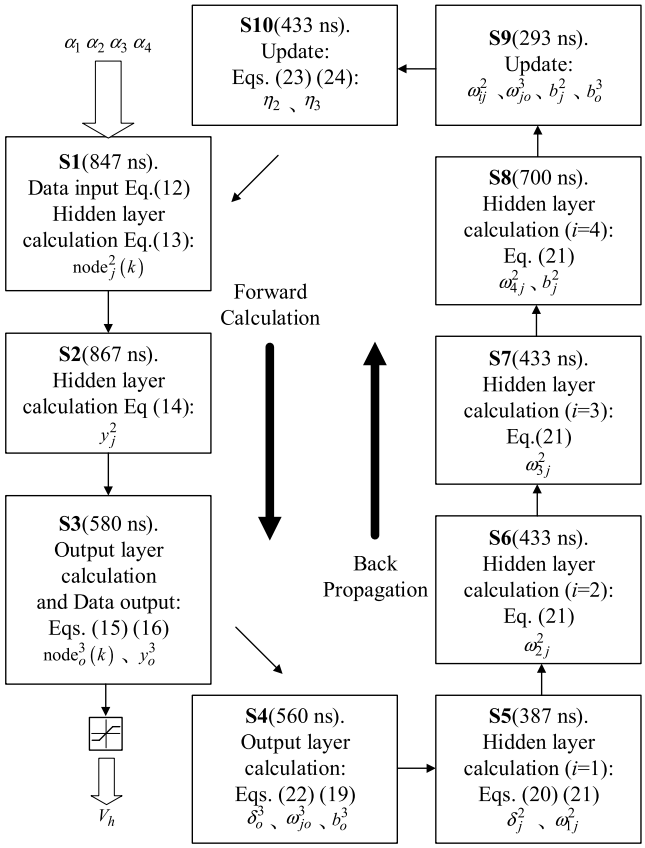

FIGURE 7 Algorithm flow

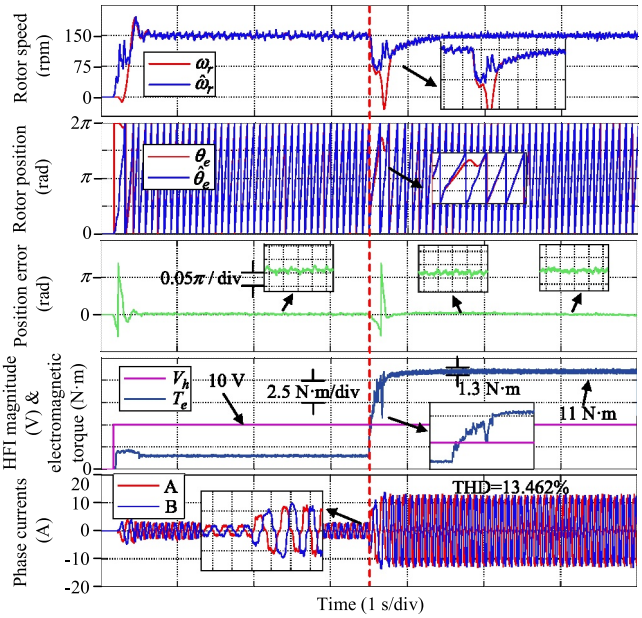

FIGURE 8 Motor start-up with step load change under conventional method with 10 V high-frequency (HF) signal injection

position error can be limited within 0.05 π. However, when the motor starts up or under step load changing, the position tracking almost fails when the magnitude of injected signal is set as 10 V. The motor even reverses when the load changes to

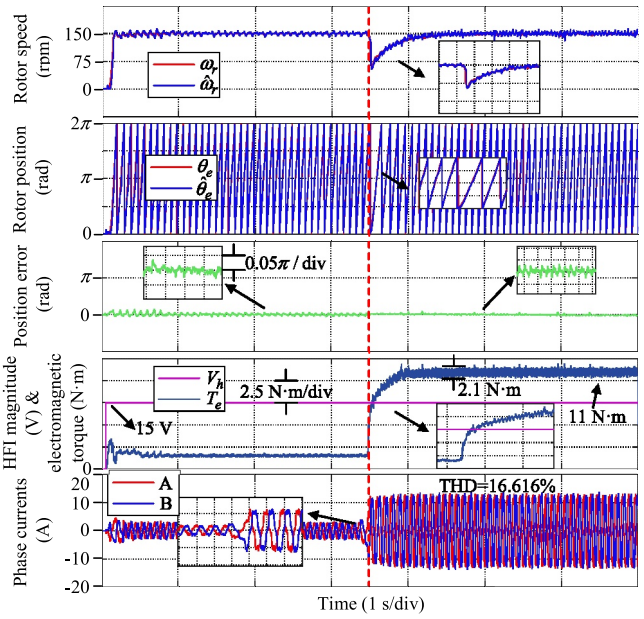

FIGURE 9 Motor start-up with step load change under conventional method with 15 V high-frequency (HF) signal injection

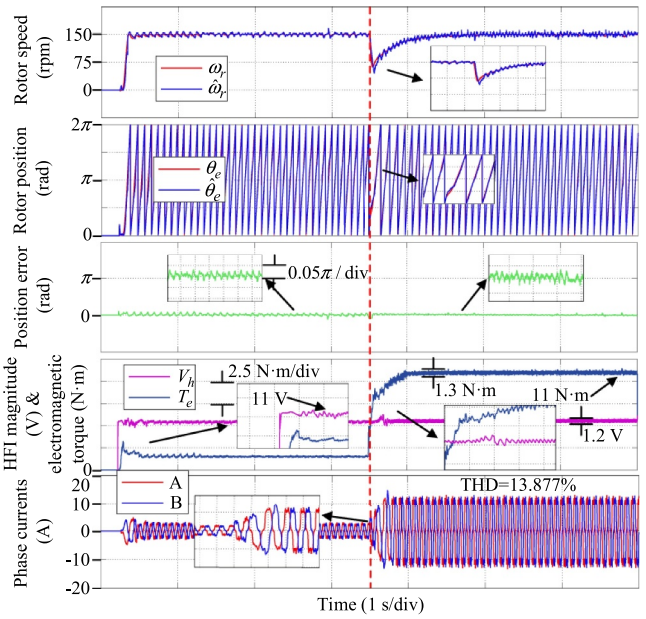

FIGURE 10 Motor start-up with step load change under proposed method with variable high-frequency (HF) signal injection

11 nm. It can be concluded that the excessive low injected voltage will cause the failure of position tracking, and the same conclusion is also confirmed in Ref. [11]. However, because of the lower voltage injection, the performance of the electromagnetic torque and phase current responses become better. The torque ripple under 10 V voltage injection is limited within 1.3 nm while that of the 15 V voltage injection is limited within 2.1 nm. The total harmonic distortion (THD) reduces from 16.616%, with 15 V voltage injection, to 13.462%, with 10 V injection. These improvements of torque performance and THD are mainly caused by the decrease of current ripple due to the lower voltage injection. It seems that 10 V is near the critical voltage of the test motor. For the better position tracking performance, the following conventional method-based experiments both adopt 15 V as the magnitude of injection.

Second, compared with Figures 8 and 9, Figure 10 shows the motor runs at better performance in both position error and torque ripple under load changing. In the one hand, at the steady-state performance, the position error is limited within 0.05π, which is the same as the conventional method. The magnitude of the injected signal is almost 11 V with slightly fluctuating within 1.2 V. When the load changes from 2 to 11 nm, the magnitude increases and back to stable soon. In other words, the magnitude could adjust the position error, which is influenced by the sudden load changing and guarantee large enough current responses for position tracking. On the other hand, the performances of the electromagnetic torque and phase current responses are almost the same as the conventional method with 10 V voltage injection, which is better than that of the conventional method with 15 V voltage injection.

It is also worthy noticing that the magnitude of injection in Figure 10 is fluctuating around 11 V and is limited within 1.2 V at steady-state. It will bring some unfavourable impacts on the current responses, especially on $K(\Delta\theta_e)$, but still under the adjustment capabilities of the PLL. In fact, $K(\Delta\theta_e)$ could be influenced by some factors such as the varying of the inductances of the motor (L_d, L_q) and inverter non-linearity mentioned above [11]. However, normalisation and some robust PLL [2] could partly reduce these unfavourable impacts.

4.2 | Static performance

Figures 11, 12 and 13 show the comparison between the conventional method and the proposed method at steady-state with different loads. The load conditions in each figure are 5, 8 and 11 nm, respectively, while the speeds of the motor are all 150 rpm. The results in each group contains five aspects, which are the rotor position, the position error, the magnitude of the injected signal, the electromagnetic torque performance, and the phase current (phase A and B) responses, respectively.

It can be seen from the results that under the three load conditions, the position tracking performance of proposed method is almost the same as the conventional method. The position error is limited within 0.05 π whether under fixed 15 V signal injection or under varying ones. However, with regard to the three different load conditions, the torque performance and phase current responses have been improved under the proposed method. The torque ripples are limited within 0.7, 0.9 and 1.3 nm compared with that of the conventional method, limited within 0.9, 1.5 and 2.1 nm. It can also be seen that the performances of phase current responses are also be improved, in which the THD reduces from 16.833%, 16.683% and 16.732% to 13.726%, 13.738% and 13.658%, respectively.

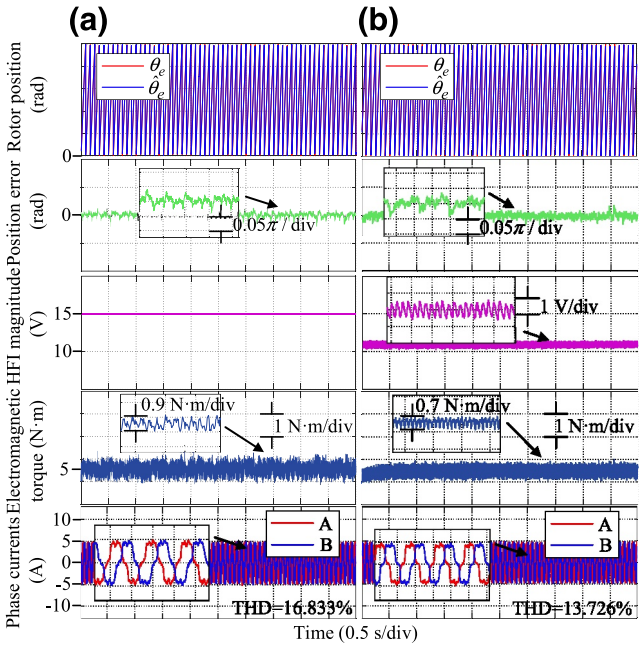

FIGURE 11 Static performance at 150 rpm with 5 nm load. (a) Conventional method. (b) Proposed method

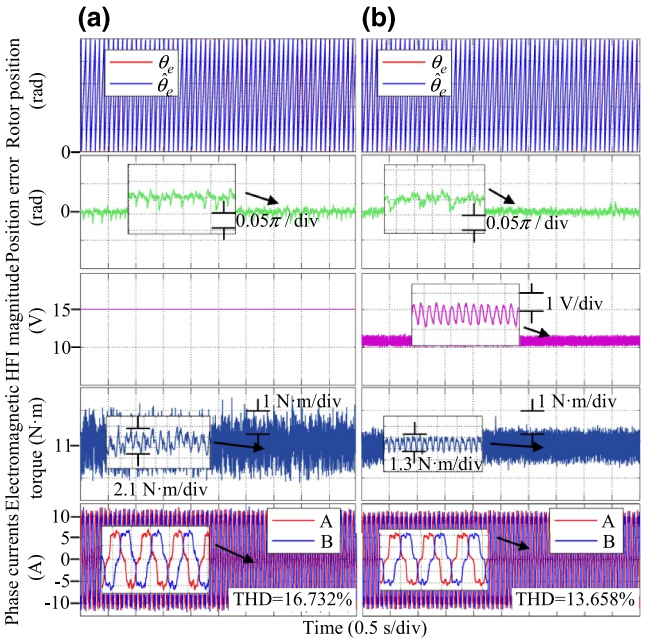

FIGURE 13 Static performance at 150 rpm with 11 nm load. (a) Conventional method. (b) Proposed method

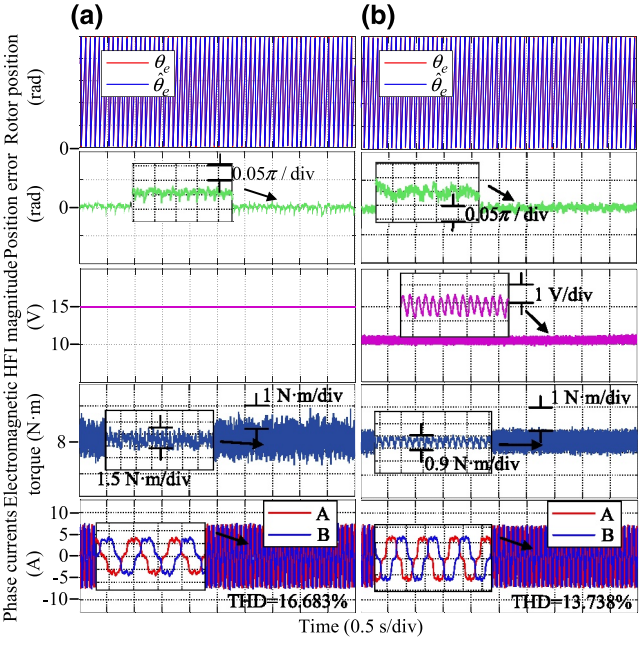

FIGURE 12 Static performance at 150 rpm with 8 nm load. (a) Conventional method. (b) Proposed method

Furthermore, the magnitude of the injected signal fluctuates around 11 V. The main reason is that the V_h calculated by the BPNN is influenced by the high-frequency current response $\hat{i}_{dh}$. According to Equations (8) (16) and (22), they both fluctuate due to the injected signal, but they are still under adjustment capabilities of the PLL. Therefore, the motor could still run steadily under the proposed method.

4.3 | Step speed change

Figure 14 shows the comparison between the conventional method and the proposed method at 11 nm load condition under three speeds, that is, 100, 150 and 200 rpm. The results in each group contain five aspects, which are the rotor speed, the position error, the magnitude of the injected signal, the electromagnetic torque performance, and the phase currents (phase A and B) responses respectively.

It can be seen that the position extraction accuracy of the proposed method is basically the same as the conventional method over the whole speed region. The position error is limited within 0.05π in both methods. The magnitude of injection is around 11 V and fluctuated within 1 V. $K(\Delta\theta_e)$ may be influenced by this unfavourable factor but still under the adjustment capabilities of the PLL, as mentioned above. The torque ripple can be reduced significantly and the performance of the current responses could be improved.

Therefore, it can be concluded that the proposed method can not only achieve high accuracy of position estimation but also significantly reduce the torque ripple to improve the torque performance of the motor.

5 | CONCLUSION

This paper proposed a BPNN-based torque ripple reduction strategy for the HF square-wave voltage-injection-based IPMSM sensorless control. First, the conventional HF square-wave voltage-injection-based IPMSM sensorless control strategy was introduced and the additional torque ripple introduced by the HF voltage signal was analysed. Second, the

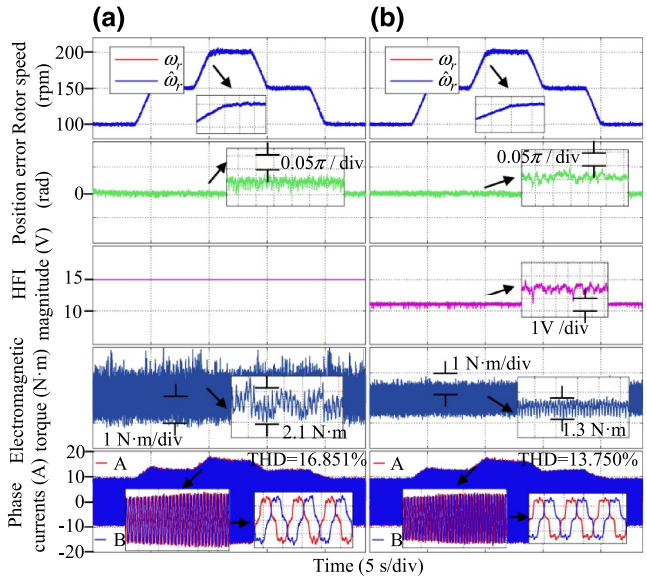

FIGURE 14 Speed change with 11 nm load. (a) Conventional method. (b) Proposed method

details of the proposed BPNN-based IPMSM sensorless control scheme were presented. The *d*-axis current and position estimation error related parameters were considered as the inputs of the BPNN, and the output of the BPNN was treated as the signal injection magnitude. Finally, the experimental results were presented to illustrate the effectiveness of the proposed scheme. With the aid of the BPNN, the optimal injection magnitude can be obtained and updated online to reduce the torque ripple as much as possible while guaranteeing the accuracy of position estimation. Compared with the conventional fixed injection magnitude, the peak-to-peak value of the torque ripple can be reduced by nearly half while the accuracy of position estimation is unchanged in the proposed scheme.

AUTHOR CONTRIBUTIONS

Yan Li—Data curation and Formal analysis. Zhen Chen—Funding acquisition and Resources. Xiaoyong Sun—Methodology and Writing—original draft. Congzhe Gao—Investigation and Software. Xiangdong Liu—Project administration and Supervision. Youguang Guo—Project administration.

ACKNOWLEDGEMENTS

Funder: National key research and development program. Grant number: BZ0388202101.

CONFLICT OF INTEREST

No authors in this paper have a conflict of interest to disclose.

DATA AVAILABILITY STATEMENT

Data openly available in a public repository that issues datasets with DOIs.

ORCID

Yan Li https://orcid.org/0000-0003-1347-0522
Xiaoyong Sun https://orcid.org/0000-0001-7175-9610

REFERENCES

1. Xu, D., et al.: A review of sensorless control methods for AC motor drives. CES Trans. Electr. Mach. Syst. 2(1), 104–115 (2018). https://doi.org/10.23919/tems.2018.8326456
2. Wang, G., Valla, M., Solsona, J.: Position sensorless permanent magnet synchronous machine drives—a review. IEEE Trans. Ind. Electron. 67(7), 5830–5842 (2020). https://doi.org/10.1109/tie.2019.2955409
3. Yildiz, R., Barut, M., Zerdali, E.: A comprehensive comparison of extended and unscented Kalman filters for speed-sensorless control applications of induction motors. IEEE Trans. Ind. Inf. 16(10), 6423–6432 (2020). https://doi.org/10.1109/tii.2020.2964876
4. Xu, Z., et al.: A nonlinear extended state observer for rotor position and speed estimation for sensorless IPMSM drives. IEEE Trans. Power Electron. 35(1), 733–743 (2020). https://doi.org/10.1109/tpel.2019.2914119
5. Xu, W., et al.: Improved nonlinear flux observer-based second-order SOIFO for PMSM sensorless control. IEEE Trans. Power Electron. 34(1), 565–579 (2019). https://doi.org/10.1109/tpel.2018.2822769
6. Almarhoon, A.H., Zhu, Z.Q., Xu, P.: Improved rotor position estimation accuracy by rotating carrier signal injection utilizing zero sequence carrier voltage for dual three-phase PMSM. IEEE Trans. Ind. Electron. 64(6), 4454–4462 (2017). https://doi.org/10.1109/tie.2016.2561261
7. Wang, X., et al.: Self-adjusting strategy based on rotating injection for sensorless control of high-power PMSM drives. In: 2019 10th International Conference on Power Electronics and ECCE Asia (ICPE 2019 - ECCE Asia), pp. 1–6 (2019)
8. Zhang, G., et al.: Pseudorandom-frequency sinusoidal injection based sensorless IPMSM drives with tolerance for system delays. IEEE Trans. Power Electron. 34(4), 3623–3632 (2019). https://doi.org/10.1109/tpel.2018.2865802
9. Wang, S., Yang, K., Chen, K.: An improved position-sensorless control method at low speed for PMSM based on high-frequency signal injection into a rotating reference frame. IEEE Access 7, 86510–86521 (2019). https://doi.org/10.1109/access.2019.2925214
10. Yoon, Y., et al.: High-bandwidth sensorless algorithm for ac machines based on square-wave-type voltage Injection. IEEE Trans. Ind. Appl. vol. 47(3), 1361–1370 (2011)
11. Kwon, Y.-C., Sul, S.-K.: Reduction of injection voltage in signal injection sensorless drives using a capacitor-integrated inverter. IEEE Trans. Power Electron. vol. 32(8), 6261–6274 (2017)
12. Zhang, G., et al.: Active disturbance rejection control strategy for signal injection-based sensorless IPMSM drives. IEEE Trans. Transport. Electr. vol. 4(1), 330–339 (2018)
13. Wang, G., et al.: Enhanced linear ADRC strategy for HF pulse voltage signal injection-based sensorless IPMSM drives. IEEE Trans. Power Electron. vol. 34(1), 514–525 (2019)
14. Tang, Q., et al.: PMSM sensorless control by injecting HF pulsating carrier signal into ABC frame. IEEE Trans. Power Electron. 32(5), 3767–3776 (2017). https://doi.org/10.1109/tpel.2016.2583787
15. Wang, G., et al.: Comparative investigation of pseudorandom high-frequency signal injection schemes for sensorless IPMSM drives. IEEE Trans. Power Electron. 32(3), 2123–2132 (2017). https://doi.org/10.1109/tpel.2016.2569418
16. Wang, G., et al.: Pseudorandom high-frequency square-wave voltage injection based sensorless control of IPMSM drives for audible noise reduction. IEEE Trans. Ind. Electron. 63(12), 7423–7433 (2016). https://doi.org/10.1109/tie.2016.2594171
17. Zhang, G., et al.: Pseudorandom-frequency sinusoidal injection for position sensorless IPMSM drives considering sample and hold effect. IEEE Trans. Power Electron. 34(10), 9929–9941 (2019). https://doi.org/10.1109/tpel.2019.2893763

18. Bianchi, N., Bolognani, S.: Influence of rotor geometry of an interior PM motor on sensorless control feasibility. In: Fourtieth IAS Annual Meeting. Conference Record of the 2005 Industry Applications Conference, 2005, vol. 4, pp. 2553–2560 (2005)
19. Bianchi, N., et al.: Comparison of PM motor structures and sensorless control techniques for zero-speed rotor position detection. IEEE Trans. Power Electron. 22(6), 2466–2475 (2007). https://doi.org/10.1109/tpel.2007.904238
20. Kano, Y.: Torque ripple reduction of saliency-based sensorless drive concentrated-winding IPMSM using novel flux barrier. IEEE Trans. Ind. Appl. vol. 51(4), 2905–2916 (2015)
21. Lin, Z., et al.: Minimization of additional high-frequency torque ripple for square-wave voltage injection IPMSM sensorless drives. IEEE Trans. Power Electron. 35(12), 13345–13355 (2020). https://doi.org/10.1109/tpel.2020.2997088
22. Li, C., et al.: Torque ripples minimization of sensorless SynRM drives for low-speed operation using Bi-HFSI scheme. IEEE Trans. Ind. Appl. vol. 68(7), 5559–5570 (2021)
23. Kim, D., et al.: Suppression of injection voltage disturbance for high-frequency square-wave injection sensorless drive with regulation of induced high-frequency current ripple. IEEE Trans. Ind. Appl. 52(1), 302–312 (2016). Jan.-Feb. 2016. https://doi.org/10.1109/tia.2015.2478887
24. Lin, F.-J., et al.: Intelligent maximum torque per ampere tracking control of synchronous reluctance motor using recurrent legendre fuzzy neural network. IEEE Trans. Power Electron. 34(12), 12080–12094 (2019). https://doi.org/10.1109/tpel.2019.2906664
25. Lin, F.-J., Hung, Y.-C., Tsai, M.-T.: Fault-tolerant control for six phase pmsm drive system via intelligent complementary sliding-mode control using TSKFNN-AMF. IEEE Trans. Ind. Electron. 60(12), 5747–5762 (2013). https://doi.org/10.1109/tie.2013.2238877

How to cite this article: Li, Y., et al.: Back propagation neural network-based torque ripple reduction strategy for high frequency square-wave voltage injection-based interior permanent magnet synchronous motor sensorless control. IET Electr. Power Appl. 1–11 (2022). https://doi.org/10.1049/elp2.12255